Journal of Science: Advanced Materials and Devices 7 (2022) 100440

Contents lists available at ScienceDirect

Journal of Science: Advanced Materials and Devices

journal homepage: www.elsevier.com/locate/jsamd

Original Article

TCO-free perovskite solar cells in taking advantage of SWCNT/TiO_2 core/shell sponge

Hong-Cuong Truong [a], Cong-Dan Bui [a], Van-Duong Dao [b], Sy-Hieu Pham [c], Philippe Leclère [c], Duy-Cuong Nguyen [a], Bui-Thi Hang [a], Van-Quy Nguyen [a], Van-Dang Tran [a, *], Soon-Gil Yoon [d, **]

[a] International Training Institute for Materials Science, Hanoi University of Science and Technology, Hanoi, Viet Nam
[b] Faculty of Biotechnology, Chemistry and Environmental Engineering, Phenikaa University, Hanoi, 10000, Viet Nam
[c] Laboratory for Physics of Nanomaterials and Energy, Research Institute in Materials Science and Engineering, University of Mons (UMONS), B-7000 Mons, Belgium
[d] Department of Materials Science and Engineering, Chungnam National University, Daejeon, 305-764, South Korea

ARTICLE INFO

Article history:
Received 17 November 2021
Received in revised form
8 February 2022
Accepted 26 February 2022
Available online 10 March 2022

Keywords:
Perovskite solar cells
SWCNT/TiO_2 sponge
TCO-free
CVD
Dual functions

ABSTRACT

A nanohybrid of titanium dioxide (TiO_2) and single-walled carbon nanotubes (SWCNTs) with dual functions of collecting electrons and transparent electrode layer is synthesized by nano-cluster deposition technology. The super-hollow structure of the SWCNTs was directly fabricated via arc discharge and fully covered with a thin layer (~15 nm) of TiO_2, which formed the SWCNT/TiO_2 core/shell sponge. The developed SWCNT/TiO_2 core/shell sponge is used directly as scaffolding for a light absorber and electron collector in transparent conducting oxide (TCO) electrode-free perovskite solar cells (PSCs) for the first time, which exhibited a power conversion efficiency of 7.2%. The large surface area of the core/shell bundle is sufficiently effective in transferring the photogenerated electron from the Perovskite absorber to the SWCNTs. More importantly, the findings of this work could support the concept of replacing the conventional TCO in PSCs and pave the way to further work for developing inexpensive and flexible PSCs.

1. Introduction

In 2009, the first report on perovskite solar cells (PSCs) based on $CH_3NH_3PbI_3$ ($MAPbI_3$) and $CH_3NH_3PbBr_3$ ($MAPbBr_3$) was first introduced with a power conversion efficiency (PCE) of 3.8% [1]. Note that the first structure of PSC is based on a liquid-junction photovoltaic (PV) device [1]. In 2012, Park et al. presented for the first time, the solid-state mesoscopic heterojunction solar cells employing nanoparticles (NPs) of methylammonium lead iodide $(CH_3NH_3)PbI_3$ as light harvesters with a PCE of 9.7% [2]. After just a century of research, the highest PCE is recorded and certified to over 25.5% [3]. The PCE of PSC is comparable to that of other commercialized solar cells, such as multicrystalline Si (c-Si, 23.3%), cadmium telluride (CdTe, 22.1%) and copper indium gallium selenide (CIGS, 23.4%) solar cells [4]. However, to facilitate the commercialization of PSCs, various issues must be addressed, such as long-term stability, Pb-free, low-cost manufacturing process, and a simple implementation for making flexible panels that have diverse applications [5]. Among factors, the competitive price of PSCs becomes the most important, which results from the low material cost and non-vacuum fabrication process. The relatively high material costs come from metallic electrode materials and transparent conducting oxide (TCO) such as indium-doped tin oxide (ITO) or fluorine-doped tin oxide (FTO) substrate. Because the cost of HTM is expected to decrease by virtue of new methods or large-scale synthesis methods, even now, the PSC can be fabricated with HTM-free [6,7]. Gold and FTO glass have a similar cost of $40 per g. Note that gold electrode can be replaced by carbon electrode [8]. However, a significant reduction in the price of FTO and ITO electrodes seems to be not considered yet.

Recently, carbon nanotubes (CNTs) have received increasing attention due to outstanding mechanical, optoelectronic, and

* Corresponding author.
** Corresponding author.
E-mail addresses: dang.tv@itims.edu.vn (V.-D. Tran), sgyoon@cnu.ac.kr (S.-G. Yoon).

Peer review under responsibility of Vietnam National University, Hanoi.

https://doi.org/10.1016/j.jsamd.2022.100440

chemical properties, which are required for many viable applications [9]. As compared with ITO and FTO films, CNT film has several advantages such as abundance, high flexibility, and stability in the presence of either an acid or a base. These unique properties suggest that CNT film could be a possible replacement for TCO electrodes in flexible electronics, particularly for PV technology [10]. In fact, CNT films have been used as a transparent electrode for organic PV cells and dye-sensitized solar cells (DSCs) [11–16]. In particular, for applications in PSC devices, single-walled CNT (SWCNT) films have recently been employed as both a hole-collecting layer and the top electrode for good performance and highly stable cells [17].

Based on these backgrounds, we introduce here for the first time the fabrication of PSCs with TCO-free electrodes. For this purpose, the SWCNT/TiO_2 core/shell sponge fabricated via nano-cluster deposition (NCD) is employed as an FTO/TiO_2 blocking layer. Moreover, the SWCNT/TiO_2 sponge structure also takes the role of the mesoporous scaffold for the light absorber material. The optical and electrical properties of SWCNT/TiO_2 core/shell are investigated for their feasibility in PSCs. As a result, a PCE of 7.2% was achieved. It should be emphasized that although efficiency was quite low, the concept without using TCO is expected to provide an important development in the electrode study of PSCs.

2. Experimental

2.1. Deposition of SWCNTs and thin TiO_2 films onto SWCNTs for an SWCNT/TiO_2 core/shell

SWCNTs were deposited onto a glass substrate for use as the inner-core electrode. The substrate was 1.5 × 1.5 cm^2 in size and was mounted on the wall of an arc-discharge chamber for *in situ* SWCNT deposition. A graphite rod was used as the carbon source. The synthesis of SWCNTs was performed under optimized conditions with an arcing current density of 85 A/cm^2 for 6 min under 5.3 × 10^4 Pa ambient hydrogen for 6 min. Because as-deposited SWCNTs contain an amorphous carbon, they were annealed at 400 °C for 30 min for purification and then covered by a shadow mask (1.5 × 0.2 cm^2) for measurement connection. To produce an SWCNT/TiO_2 core/shell, a thin TiO_2 layer was deposited onto the SWCNTs via NCD. Note that the detailed NCD technique was described in previous work [18]. TiO_2 was deposited via NCD-using $Ti(O\text{-}iPr)_2$ $(dibm)_2(Ti(Oi{-}C_3H_7)_2(C_9H_{15}{-}O_2)_2)$ precursors as the sources of titanium, which were dissolved in hexane at concentrations of 0.075 M. The solution was injected into a vaporizer. Then it was immediately vaporized and carried to the showerhead by an argon carrier gas at a flow rate of 100 sccm (standard cc min^{-1}). The oxygen was supplied to the showerhead as a reaction gas at a fixed flow rate of 100 sccm. To prevent the condensation of the precursor vapor, the showerhead temperature was maintained at 350 °C, while the substrate temperature was maintained at 400 °C for crystallization of the TiO_2. The thickness of TiO_2 film-coated SWCNTs was measured via scanning electron microscopy (SEM) (TOPCON DS-130C) and transmission electron microscopy (TEM).

2.2. Fabrication of PSC devices

For the preparation of the perovskite dye ($MAPbI_3$), a two-step process was performed via a combination of solution and vapor deposition technique. For the optimized loading of $MAPbI_3$ onto the SWCNT/TiO_2 sponge, a PbI_2 layer was first coated onto the sponge via chemical vapor deposition (CVD) and then CH_3NH_3I (MAI) was coated onto the PbI_2 layer via spin -coating for reacting to form $MAPbI_3$ crystalline. The $MAPbI_3$ layer on the reference device was deposited by spin -coating alone onto an FTO substrate. The first step of the spin -coating, involved a 400 mg/mL PbI_2 (Sigma) solution that incorporated N, N-dimethylformamide (DMF) that was spin-coated onto the *m*-/*bl*-TiO_2/FTO and the SWCNT/TiO_2 sponge and then dried at 80 °C for 15 min. A low concentration of MAI solution (2 mg/1 mL) was spin-coated at 2000 rpm for 5 s onto the PbI_2-coated *m*-TiO_2 layers followed by a high concentration of MAI solution (40 mg/1 mL) that was dropped onto the samples and let stand for 3–4 minutes to promote the reaction between PbI_2 and MAI to form $MAPbI_3$ at room temperature. The samples were spun at 2500 rpm for 25 s. After spin coating, the samples were annealed under an argon atmosphere at 100 °C for 1 h via RTA (rapid thermal annealing). $MAPbI_3$ dye was deposited via CVD and the schematics of the process are shown in Fig. S1. For two-step deposition, PbI_2 and MAI were separately deposited under a small quartz tube with a 0.5-inch diameter that was placed into a 2.0-inch quartz tube furnace (KJMTI OTF1200X). The 300 mg of MAI and 150 mg of PbI_2 were placed into separate crucibles inside big and small tube furnaces, respectively, to confine the vapor. The SWCNT/TiO_2 sponge layer on the glass substrates was placed in the down-flow at the left of zone 2 at 120 °C. In the first step, the temperature of zone 1 (PbI_2 source) was gradually ramped up to 300 °C, and then the Ar flow rate was begun at 100 sccm. The deposition time was 15 minutes for a 100 nm thickness of PbI_2 that would cover the SWCNT/TiO_2 core/shell. The CVD method of MAI deposition was performed according to the melting point temperature, and the crucible containing MAI was placed 10 cm from the center of zone 1, where the temperature measured 140 °C and the Ar carrier gas was controlled at 150 sccm using a deposition time of 30 minutes. After fabrication of the perovskite layer, the *in-situ* annealing process was performed in the second zone of the furnace immediately after deposition at 100 °C for 60 minutes. The combined method involved the first step of PbI_2 deposition via CVD and then spin-coating the MAI deposit as mentioned above. After cooling, hole transport layers (HTL) were deposited via spin coating at 4000 rpm for 5 s on all samples using a hole transport solution that employed a spiro-OMeTAD/chlorobenzene (180 mg/1 mL) solution with the addition of 50 μL Libis (trifluoromethanesulfonyl) imide (Li-TFSI, Sigma)/acetonitrile (170 mg/1 mL) and 20 μL tert-butylpyridine (tBP, Sigma). Finally, 80 nm-thick Au films were deposited as counter electrodes via dc (direct current) sputtering under a working pressure of 0.4 Pa (base pressure of 5 × 10^{-3} Pa) using a 2-inch diameter gold target. The active area of the cell was approximately 0.25 cm^{-2}.

PSC devices with SWCNT/TiO_2 (core/shell)/$MAPbI_3$/Spiro-OMeTAD/Au and FTO/*bl*-/*m*-TiO_2/$MAPbI_3$/Spiro-OMeTAD/Au structures were fabricated for comparison. The fabrication process for the reference device on a FTO substrate has been reported by our group [19]. A 50 nm thickness of *bl*-TiO_2 was deposited via NCD onto a cleaned FTO electrode (12 Ω/□, Solaronix TCO30-8). Then the 300 nm-thick mesoporous *m*-TiO_2 was deposited onto the *bl*-TiO_2via spin coating (3000 rpm for 40s) using TiO_2 paste (Dyesol 18NR-T), which was diluted further with methanol at a ratio of 1:10 by weight. The *m*-TiO_2 layers were sintered under an air atmosphere at 450 °C for 30 min.

2.3. Characterization & measurement of the PCS devices

Optical transmittances of the SWCNT/glass and the FTO/glass were measured using S-3100 UV-vis spectroscopy. Photoluminescence (PL) spectra were recorded on UV-VIS-NIR Spectrofluorometer (JASCO FP 8600- Japan) under excitation wavelength at 300 nm. The resistivity, Hall mobility, and carrier density were measured using a four-point probe method and Hall-effect measurement of the van der Pauw geometry (HL-5500PC, Accent). The X-ray diffraction system (XRD, Rigaku D/MAX-RC) with Cu Kα radiation and a nickel filter were used to study the crystal structure.

The surface morphologies of the SWCNT/TiO_2, perovskite dye, and the cross-sectional images of the solar cell devices were analyzed using SEM. Photocurrent-voltage (I–V) characteristics of the solar cells were measured using an IVIUMSTAT under illumination from a Sun 3000 solar simulator composed of 1000 W mercury-based Xe arc lamps and AM 1.5-G filters. Light intensity was calibrated with a silicon photodiode. The measurements of I–V, Nyquist, and external quantum efficiency (EQE) of the solar devices were performed after 12 h under ambient.

The blocking effect of TiO_2 on SWCNTs was investigated via cyclic voltammetry (C–V) under a three-electrode system with a Hg/HgCl reference electrode and a platinum mesh counter electrode. The data were recorded by a computer-controlled potentiostat (Solartron SI 1286, UK). For the C–V scan, an aqueous electrolyte solution containing 0.5 mM potassium hexacyanoferrate (II) and 0.5 mM potassium hexacyanoferrate (III) with 0.5 M KCl was the supporting electrolyte. All scan rates of C–V measurements were performed at 50 mV/s.

3. Results and discussion

The use of carbonaceous materials in the semiconducting oxide scaffolds previously led to a significant enhancement in the efficiency of DSCs [20]. Therefore, in this work, we replaced the FTO electrode and the electron transport layer with an SWCNT/TiO_2 core/shell. A schematic of the SWCNT/TiO_2 perovskite solar cell structure appears in Fig. 1a. The unique cell in this study consisted of an SWCNT inner core for the role of the transparent electrode and a thin-cell TiO_2 for both a hole-blocking layer and electron transport from the perovskite light absorber to the CNT. To complete the cell, perovskite $MAPbI_3$ films were loaded onto the porous SWCNT/TiO_2 scaffold, which was followed by the sequential deposition of the hole transport material (HTM) using the spiro-OMeTAD and an Au metal electrode. SWCNTs show metallic properties with the work function between −4.6 and −4.9 eV at room-temperature [21]. Accordingly, the charge transfer process of the PSCs based on SWCNTs/TiO_2/$MAPbI_3$/spiro-OMeTAD/gold is illustrated in Fig. 1b. It shows that SWCNT can function as the anode in replacing FTO due to favorable energy alignment.

The SEM surface and cross-sectional images of the SWCNTs, synthesized via arc discharge, appear in Fig. 2a and b, respectively. The synthesized SWCNT sponges with diameters of 3 nm and lengths of tens to hundreds of micrometers are self-assembled into a super-porous, interconnected, and three-dimensional framework [18]. The as-synthesized SWCNTs included amorphous carbons as major impurities in SWCNTs. Heat-treatment at 400 °C for 30 min under ambient air was performed for the CNT purification. The heat-treated SWCNT films showed sufficient crystalline qualities, as confirmed by Raman spectroscopy (Fig. S2). Fig. 2c and d show the morphologies of the SWCNT frameworks uniformly covered by TiO_2 as-deposited films via NCD. All of the welded junctions were fully covered, but the morphologies of the SWCNT/TiO_2 core/shell structures were not dense. In order to improve the dense of SWCNT/TiO_2 films, Methanol treatment of the core/shell structure is performed, and the results are presented in Fig. 2e and f. As can be seen, the thickness of the SWCNT/TiO_2 films was decreased from 5 μm to 500 nm, as shown in Fig. 2d and f, respectively. The SWCNT/TiO_2 sponges had a high level of porosity due to the advantage of a great amount of surface area, which also resulted in excellent mechanical strength and flexibility.

The thickness and crystallinity of the TiO_2 shells were further investigated via TEM and XRD, as shown in Fig. 3. As can be seen in Fig. 3a, a TiO_2 film with a thickness of 15 nm was successfully deposited on the surface of SWCNTs by NCD technology. The inset Fig. 3a shows the magnified images of the shell region, which were obtained by inverse fast Fourier transform (FFT) using the selected major diffraction spots from the FFT-obtained digital diffraction patterns. It was clearly observed the lattice spacing of TiO_2 is 0.35 nm which is in good agreement with anatase TiO_2 (101) (JCPDS card no. 21–1272). The anatase phase was clearly ascertained via the XRD pattern of SWCNT/TiO_2, as shown in Fig. 3b.

C–V was used to probe the blocking effect and electron transfer kinetics of an SWCNT/TiO_2 scaffold with a reference to bl-TiO_2/FTO. Aqueous $Fe(CN)_6^{3-/-4}$ solution is typically used as the model redox system in a three-electrode electrochemical cell, in which bare FTO, bl-TiO_2/FTO, SWCNT, and SWCNT/TiO_2 act as the working electrode. Via a scanning C–V of the working electrode in an aqueous $Fe(CN)_6^{3-/-4}$ electrolyte solution, the C–V representing the redox reaction between $Fe(CN)_6^{-3}$ and $Fe(CN)_6^{-4}$ was interpreted and used to determine the blocking effect of the TiO_2 layer [22]. Fig. 4a shows the C–V waves of bare FTO and SWCNT film electrode. Both electrodes showed the cathodic and anodic peak potential of a Nernstian peak voltammogram. The theoretical peak-to-peak separation value (△Ep) is 56.0 mV for a one-electron reversible reaction [23]. In this study, the △Ep values were 279 and 466 mV for the C–V waves of FTO and SWCNT electrodes, respectively. The deviation of △Ep between the theoretical and experimental values was attributed to the uncompensated resistances of the solution, wiring, and electric contacts that were not considered in the theoretical calculation. According to the classic work of Nicholson,

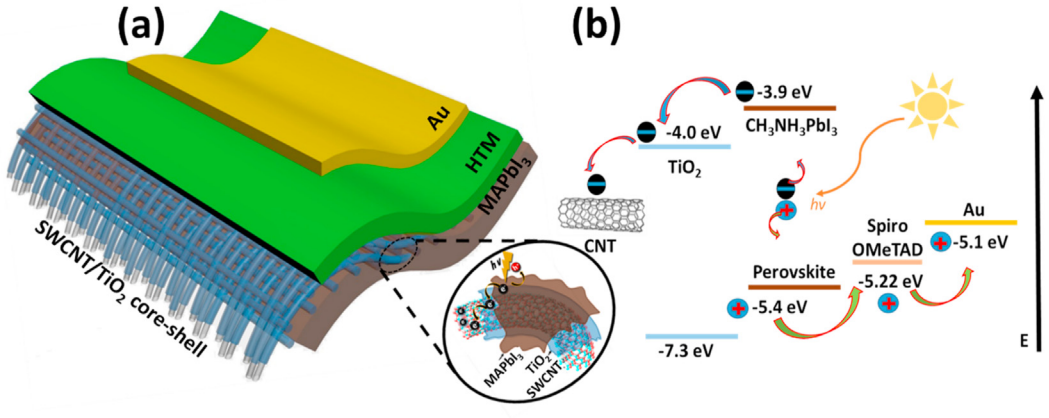

Fig. 1. (a) Schematic image of SWCNT/TiO_2 sponge perovskite solar cells and (b) Energy band diagram of the different functional layers in PSCs.

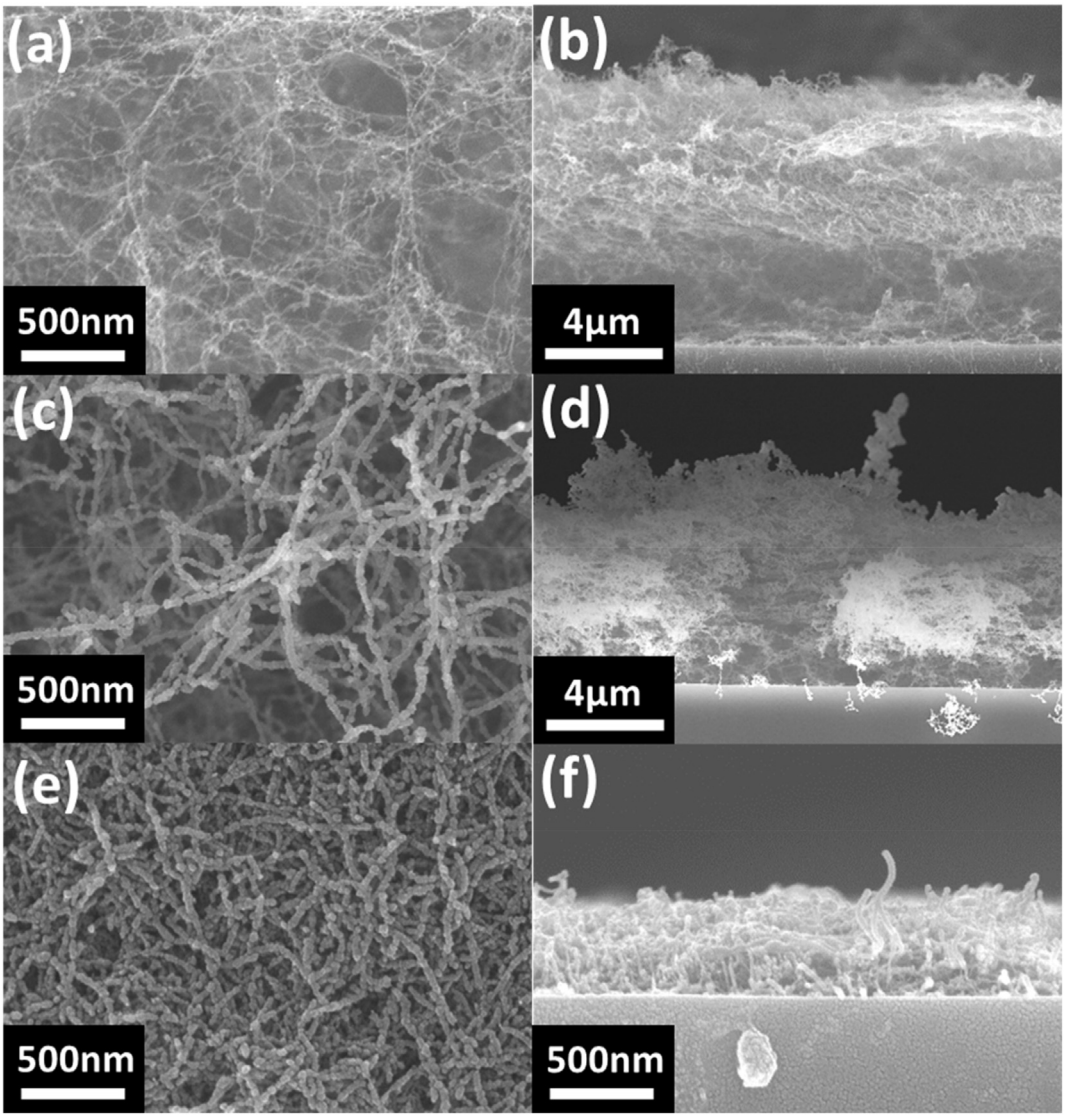

Fig. 2. SEM surface and cross-sectional images of (a, b) as-deposited SWCNT, (c, d) SWCNT/TiO_2 core/shell with thin TiO_2 deposited via NCD, and (e, f) SWCNT/TiO_2 core/shell after methanol-treatment, respectively.

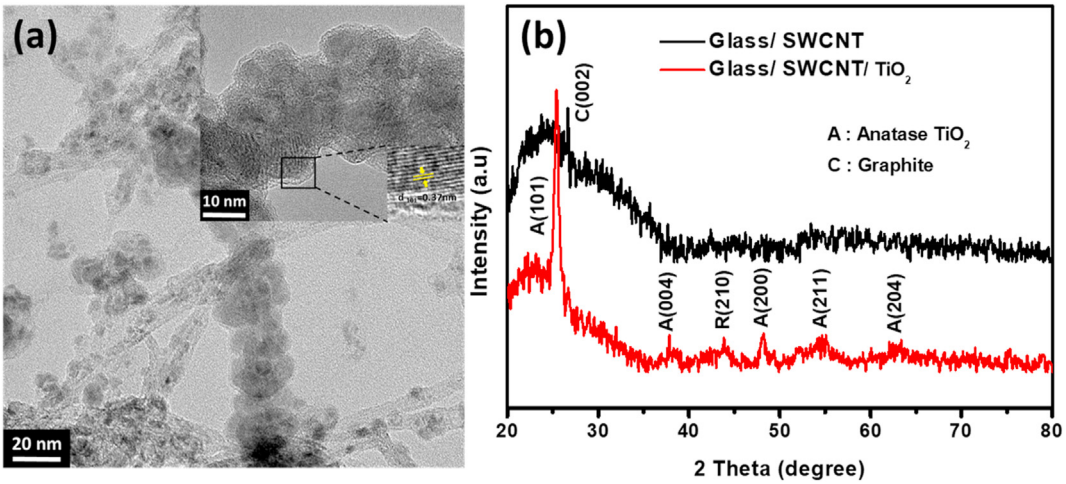

Fig. 3. (a) TEM image and (b) XRD pattern of the SWCNT/TiO_2 core/shell structure.

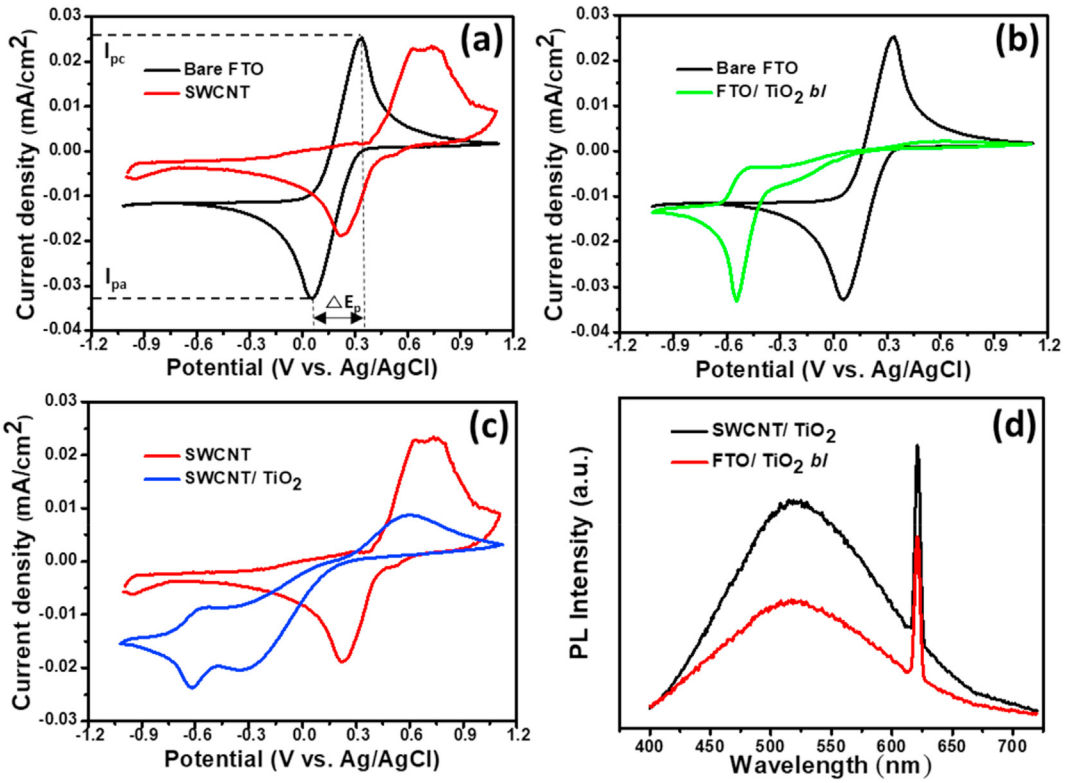

Fig. 4. C-V waves of (a) FTO and SWCNT, (b) FTO and FTO/*bl*-TiO_2, (c) SWCNT and SWCNT/TiO_2 core/shell structure, (d) Photoluminescence spectra of SWCNT/TiO_2 and FTO/*bl*-TiO_2 with the excitation wavelength at 300 nm.

the △Ep and the charge-transfer rate constant are quantitatively related [24], and that relationship was used to explain the increase in △Ep of the *C*−*V* waves of SWCNT film electrodes. The high resistivity and low charge mobility of SWCNT-film (Table S1) reduced the charge transfer kinetics. The relatively low-quality SWCNT synthesized by arc discharge method is due to the remaining amorphous carbon and metal oxides catalyst. This impurity not only leads to lower conductivity but also changes the work function of SWCNT. The symmetry of the cathodic and anodic peaks indicates that the redox of $Fe(CN)_6^{3-/-4}$ ions possessed electrochemical reversibility on the bare FTO and SWCNT film, which indicated there was no blocking effect. The green line in Fig. 4b is the *C*−*V* wave of FTO with *bl*-TiO_2. Based on a low peak current density, the anodic reaction was blocked. This result showed that the oxidation of $Fe(CN)_6^{3-}$ was hindered because it required potentials above 0.24 V when the TiO_2 was switched back to its insulating state. The redox potential of $Fe(CN)_6^{3-/4-}$ (0.24 V vs Ag/AgCl) was sufficiently positive to the flat-band potential of TiO_2 anatase at all practically accessible pH values in the aqueous electrolyte solutions [25]. Titania behaves similarly to an electrochemically silent dielectric material against the $Fe(CN)_6^{3-/4-}$ pair. In this case, the charge transfer reaction was assumed to have occurred solely at the surfaces of the naked electrodes, which were exposed to the electrolyte solution through pinholes. Therefore, the effective pinholes are evaluated by the peak current density, I_p, which is given by the Randless-Sevcik equation:

$$I_p = k \times n^{3/2} \times A \times c \times D^{1/2} \times v^{1/2} \quad (1)$$

where k is a constant ($k = 2.69 \times 10^5$ C mol^{-1} V $^{-1/2}$), n is the number of electrons transferred in the redox couple, A is the electrode area, D is the diffusion coefficient, and v is the scan rate. The equation (1) assumes that peak current density is proportional to the electrode area, A. When the FTO surface is coated by *bl*-TiO_2, the electrode area that is available for the reaction is reduced, accordingly leading to a decrease in the I_p. The I_p is the peak current density measured using the actual *bl*-TiO_2/FTO electrode (uncovered area of FTO is indicated as "*A*") and I_{po} is the current density measured using the bare FTO electrode area (A_o). The effective pinhole area can be described as follows:

$$A/A_o = I_p / I_{po} \quad (2)$$

The ratios calculated from the C-V results of *bl*-TiO_2/FTO and SWCNT/TiO_2 were 0.089 and 0.37, respectively, indicating blocking effects of 91.1 and 63.0%, which is a coverage percentage equal to that of the TiO_2 layers on FTO and SWCNTs. The C-V analysis suggested that the TiO_2 deposited on FTO via NCD exhibited an excellent blocking effect. In contrast, SWCNT/TiO_2 core/shell structures have some defects that originate from the raw SWCNTs that remain uncovered by *bl*-TiO_2, which degraded the PV performance of the PSCs.

To further examine the efficiency of charge carrier trapping and transfer in these types of electrodes, the photoluminescence emission spectrum of SWCNT/TiO_2 sponge and FTO/TiO_2 were recorded and shown in Fig. 4d. Under excitation at wavelength of 300 nm, it could be observed that there are two emission peaks in PL spectra of both samples. The broad peak that appeared around 518 nm (~2.4 eV) corresponded with recombination of photogenerated holes and electron. The second emission peak at 620 nm (~2.0 eV) resulted from the oxygen vacancies in TiO_2 material [26]. The SWCNT and FTO showed no peaks due to their metallic properties. From the PL spectra, it was confirmed that the difference in charge transfer kinetics leads to the changes in the PL peak

intensity [27,28]. The low conductivity of SWCNT leads to a higher intensity of emission peak, suggesting the higher the recombination rate of charge carriers. The decrease in PL peak intensity of FTO/TiO_2 sample is because of excellent carrier mobility which could promote the efficient separation of charge carriers, thus benefiting in PV performance [29].

Sufficient infiltration of the $MAPbI_3$ perovskite absorber into the SWCNT/TiO_2 scaffold was considered a challenging process. The filling of the pores is the main factor that can be used to enhance the charge percolation pathway. The perovskite was filled on the porous scaffold, and it also formed a compact capping layer on the SWCNT/TiO_2 structure that achieved high PSC performance. SWCNT/TiO_2 is a super-porous structure with a large space for perovskite loading. However, the weak adhesion of the SWCNT/TiO_2 to substrates combined with the hydrophobic properties of SWCNTs made by spin coating is impossible for perovskite deposition. As shown in Fig. S3, the perovskite was deposited onto SWCNT/TiO_2 via the two-step spin-coating process as used in our previous work [19]. The perovskite's particulate networks accumulated on the surface of the SWCNT/TiO_2 sponge. Therefore, the sufficient coverage of the perovskite dyes within the SWCNT/TiO_2 was a critical point for this study. Filling the pores in the sponge structure by overcoming the hydrophobicity of SWCNT/TiO_2 was enhanced via CVD for perovskite dye deposition. The two-step process for perovskite deposition via CVD, however, also exhibited the limitations, as shown in Figs. S3c and S3d. First, the PbI_2 layer was deposited on the surface of the SWCNT/TiO_2 core/shell, and then MAI was deposited to react with PbI_2 to form $MAPbI_3$ perovskite. In the sequentially deposited perovskite film, separated crystal particles with a cubic shape appeared on the compact structure. Both the devices derived from these methods possessed very poor PV performance with strong I–V hysteresis (Fig. S4). As a solution for these problems, we selected a process that combined CVD and a solution technique for the conformal and homogeneous deposition of a significant perovskite capping layer. According to the developed method, the SWCNT/TiO_2 film (Fig. 5a) was first coated a PbI_2 layer. The obtained result is presented in Fig. 5b. Next, the MAI solution was spin-coated onto an SWCNT/TiO_2/PbI_2 film for the growth of $MAPbI_3$ films on the surface of SWCNT/TiO_2. Fig. 5c and d show the SEM surface and cross-sectional images of perovskite/SWCNT/TiO_2/glass deposited via a combined process. Based on the morphological aspects, this combined method was the most effective in achieving a capping over-layer for coverage of the SWCNT/TiO_2 core/shell. Fig. 5d shows the cross-sectional SEM image of a full solar-cell device. The sequentially deposited device shows a dense layer onto which the HTM was coated to create a flat and homogeneous surface covering the perovskite light absorber. The HTM, the perovskite capping layer, and the SWCNT/TiO_2 layer are apparent in the cross-sectional image.

The PV performance of the PSC devices fabricated on FTO and SWCNT/TiO_2 under AM1.5 G illumination is illustrated in Fig. 6a. As can be seen, PSC devices based on SWCNT/TiO_2 electrode had a short-circuit currents (J_{sc}) of 14.0 mA/cm^2, an open circuit voltage (V_{oc}) of 0.82 V, a Fill Factor (*FF*) of 0.63, and a PCE of 7.2%. Note that the PSC devices composed of *m*-/*bl*-TiO_2/FTO showed a J_{sc} of 20.6 mA/cm^2, a V_{oc} of 1.04 V, an *FF* of 0.71, and then yielded a PCE of 15.2% in a backward scan from forwarding bias to short circuit. To further elucidate the difference in J_{sc} values, the incident photon-to-electron conversion efficiency (IPCE) for all devices are conducted. The EQE is an important parameter for evaluating the performance of solar cells. The EQE characteristics of conventional PSC devices fabricated on *m*-/*bl*-TiO_2/FTO and SWCNT/TiO_2 electrodes are shown in Fig. 6b. The EQE spectra and integrated J_{sc} showed good agreement with the trend observed for the J_{sc}. The cells fabricated with an SWCNT/TiO_2 sponge showed a shape similar to the FTO-based PSC, but with a lower EQE value. Under illumination, both devices responded to a wavelength that ranged from 300 to 800 nm, indicating that the use of SWCNT films did not

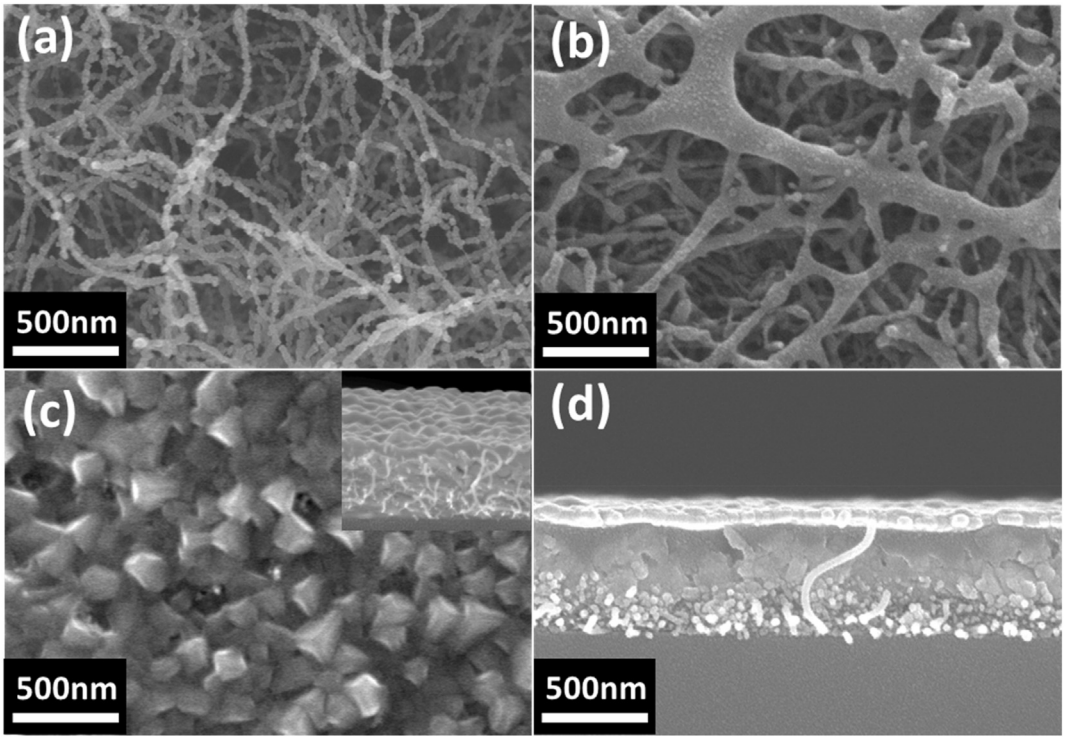

Fig. 5. SEM surface images of (a) SWCNT/TiO_2, (b) PbI_2/SWCNT/TiO_2, and (c) $MAPbI_3$/SWCNT/TiO_2. (d) SEM cross-sectional image of full-cell structure of Au/HTM/$MAPbI_3$/SWCNT/TiO_2/Glass.

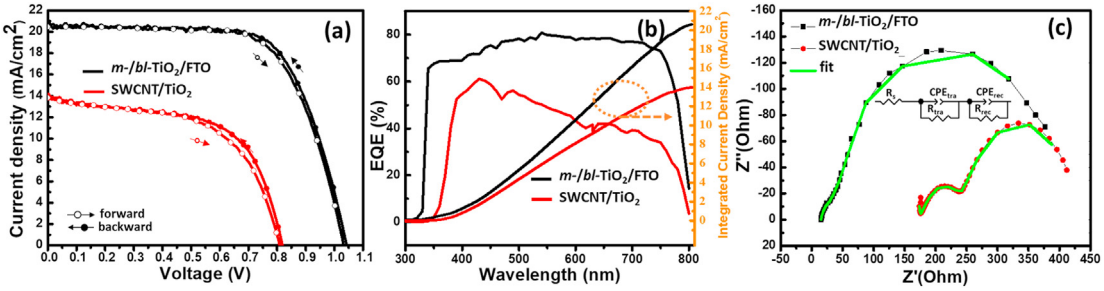

Fig. 6. (a) Photocurrent-voltage curve, (b) External Quantum efficiency and short-circuit current density calculated by EQE, and (c) Electrochemical impedance spectroscopy of PSC devices with *m*-/*bl*-TiO_2/FTO and SWCNT/TiO_2 core/shell.

alter the internal mechanism of the PSCs. The ~800 nm cut-off wavelength corresponds to the 1.55 eV band gap of the $MAPbI_3$ perovskite absorber. The lower EQE for the SWCNT/TiO_2 cell was considered the result of poor charge collection, which was due to the limitations of absorber loading onto the sponge structure and to a level of high interface resistance between TiO_2 and SWCNTs. The FTO-based device provided pinhole-free *bl*-TiO_2 and effective coverage of the perovskite capping layer, and, therefore, it prevented a short contact between the bottom electrode and *n*-type TiO_2 with a *p*-type HTM layer, which resulted in the positive effect of a reduction in charge recombination that resulted in an improvement in V_{oc} (Fig. S5). The obtained result is in line with C–V measurements as well as other reports [30,31]. The disparity in FF between the two devices was attributed to the cell series and recombination resistance, which was further investigated with electrochemical impedance spectroscopy (EIS) under one sun illumination, as demonstrated in Fig. 6c. As can be seen, there are different shapes of EIS for different devices. The SWCNT-based device was separated by two semi-circles with increasing frequency. A complete model of an equivalent circuit for the structure of a PSC with a TiO_2 mesoporous scaffold has been reported by Dualed et al. [32]. Therefore, the EIS were fitted following the previously reported equivalent circuit [32]. Accordingly, the small semi-circle of impedance spectra observed at high frequency in a PSC device using the SWCNT/TiO_2 sponge was attributed to the charge transport, whereas the remainder of the semi-circle was due to charge recombination. The parameters extracted from the EIS fitting are summarized in Table 1. The R_{tra} values account for the charge transfer process, which includes the injection of electrons into the bottom electrode from TiO_2, and the hole transfer to the Au top electrode of HTM. In the FTO-based device, no clear semi-circles were evident for electron transport, which led to lower values for R_{tra}. This result was attributed to a low-level mismatch in the energy levels of the TiO_2 conduction band and the work function of FTO. The Fermi level of SWCNTs is in range from 4.7 to 4.9 eV in an ideal product; however, this value in raw SWCNT could be much varied. Thus, in this work, the SWCNT/TiO_2 core/shell structure requires a higher driving force for electron injection from TiO_2 to SWCNTs, which results in a higher R_{tra}. Another critical point concerning SWCNT-based PSCs is that the sheet-resistance (R_s) value of SWCNT-based devices is substantially higher than the FTO-based one. This is an expected consequence of the lower charge mobility of SWCNTs (Table S1). The recombination resistance (R_{rec}) clearly mirrors the shape of the *J-V* curve, showing the recombination behavior of the devices. The R_{rec} was much lower for the FTO-based devices. The decrease in the recombination rate was reflected in higher values for *FF* and V_{oc}. This observation is in good agreement with SEM images, where the *bl*-TiO_2 and perovskite capping layers showed better coverage in FTO-based devices (Fig. S5). The obtained result suggests that improvement of the SWCNT quality and process optimization can increase further the PCE of SWCNT-based devices.

Table 1
Photovoltaic performance of PSCs with *m*-/*bl*-TiO_2/FTO and SWCNT/TiO_2 core/shell structure.

Device	$V_{oc}(V)$	$J_{sc}(mA.cm^{-2})$	*FF(%)*	$R_s(\Omega)$	$R_{tra}(\Omega)$	$R_{rec}(\Omega)$	*PCE(%)*
FTO/TiO_2	1.04	20.6	71	14.9	24.6	340.6	15.2
SWCNT/TiO_2	0.82	14.0	63	173.4	78.9	169.7	7.2

4. Conclusion

A unique approach was demonstrated via the use of an SWCNT/TiO_2 core/shell sponge structure for free-TCO PSCs. The compatibility, effectiveness, and mechanism of these solar cells were examined for utility in PSC devices and they were compared with traditional FTO electrodes. Loading a perovskite absorber into the SWCNT/TiO_2 core/shell sponge structure created optimal conditions that returned a PCE of 7.2%. Although the efficiency of PSC devices with SWCNT/TiO_2 core/shell sponge was low, further PCE enhancement is expected by applying higher-quality SWCNTs for improvements in conductivity and charge mobility. This work should open new avenues for the development of low-cost flexible PSCs.

Declaration of competing interest

The authors declare that they have no known competing financial interests or personal relationships that could have appeared to influence the work reported in this paper.

Acknowledgements

This work is funded by the Ministry of Education and Training, Vietnam under the project (No. B2021-BKA-03).

Appendix A. Supplementary data

Supplementary data to this article can be found online at https://doi.org/10.1016/j.jsamd.2022.100440.

References

[1] A. Kojima, K. Teshima, Y. Shirai, T. Miyasaka, Organometal halide perovskites as visible-light sensitizers for photovoltaic cells, J. Am. Chem. Soc. 131 (2009) 6050–6051.
[2] H.S. Kim, R.L. Chang, M. Gratzel, N.G. Park, Lead iodide perovskite sensitized all-solid-state submicron thin film mesoscopic solar cell with efficiency exceeding 9%, Sci. Rep. 2 (2012) 591.
[3] M. Green, E. Dunlop, J.H. Ebinger, M. Yoshita, N. Kopidakis, Solar cell efficiency tables (version 57), Prog. Photovoltaics 29 (1) (2021) 3–15.

[4] NREL, Best research-cell efficiencies. http://www.nrel.gov/ncpv/images/%20efficiency_chart.jpg, 2021.
[5] B.J. Kim, D.H. Kim, S.L. Kwon, S.Y. Park, Z. Li, K. Zhu, H.S. Jung, Selective dissolution of halide perovskites as a step towards recycling solar cells, Nat. Commun. 7 (2016) 22735.
[6] W.A. Laban, L. Etgar, Depleted hole conductor-free lead halide iodide heterojunction solar cells, Energy Environ. Sci. 6 (2013) 3249.
[7] J. Shi, J. Dong, S. Lv, Y. Xu, L. Zhu, J. Xiao, X. Xu, H. Wu, D. Li, Y. Luo, Q. Meng, Hole-conductor-free perovskite organic lead iodide heterojunction thin-film solar cells: high efficiency and junction property, Appl. Phys. Lett. 104 (2014) 63901.
[8] A. Mei, X. Xi, L. Liu, Z. Ku, T. Liu, Y. Rong, M. Xu, M. Hu, J. Chen, Y. Yang, M. Gratzel, H. Han, A hole-conductor–free, fully printable mesoscopic perovskite solar cell with high stability, Science 345 (2014) 295–298.
[9] M.F. De Volder, S.H. Tawfick, R.H. Baughman, A. John Hart, Carbon nanotubes: present and future commercial applications, Science 339 (2013) 535–539.
[10] A. Schindler, ITO replacements: carbon nanotubes, in: J. Chen, W. Cranton, M. Fihn (Eds.), Handbook of Visual Display Technology, Springer International Publishing: Cham, 2016, pp. 1235–1255.
[11] I. Jeon, K. Cui, T. Chiba, A. Anisimov, A.G. Nasibulin, E.I. Kauppines, S. Maruyama, Y. Matsuo, Direct and dry deposited single-walled carbon nanotube films doped with MoOx as electron-blocking transparent electrodes for flexible organic solar cells, J. Am. Chem. Soc. 137 (2015) 7982–7985.
[12] P.T. Tyler, E.B. Ryan, J.K. Hunter, J.M. Tobin, C.H. Mark, Electronically monodisperse single-walled carbon nanotube thin films as transparent conducting anodes in organic photovoltaic devices, Adv. Energy Mater. 1 (2011) 785–791.
[13] R.V. Salvatierra, C.E. Carlos, R.S. Lucimara, G.Z.J. Aldo, ITO-free and flexible organic photovoltaic device based on high transparent and conductive polyaniline/carbon nanotube thin films, Adv. Funct. Mater. 23 (2013) 1490–1499.
[14] G. Dabera, K. Jayawardena, S. Ravip, Hybrid carbon nanotube networks as efficient hole extraction layers for organic photovoltaics, ACS Nano 7 (2013) 556–565.
[15] S. Kim, J. Yim, X. Wang, D.D.C. Bradley, S. Lee, C. John, Spin- and spray-deposited single-walled carbon-nanotube electrodes for organic solar cells, Adv. Funct. Mater. 20 (2010) 2310–2316.
[16] U.N. Maiti, W.J. Lee, J.M. Lee, Y. Oh, J.Y. Kim, J.E. Kim, J. Shim, T.H. Han, S.O. Kim, 25th anniversary article: chemically modified/doped carbon nanotubes & graphene for optimized nanostructures & nanodevices, Adv. Mater. 26 (2014) 40–67.
[17] K. Aitola, K. Sveinbjörnsson, J. Correa-Baena, A. Kaskela, A. Abate, Y. Tian, E.M.J. Johansson, M. Gratzel, E.I. Kauppinen, A. Hagfeldt, G. Boschloo, Carbon nanotube-based hybrid hole-transporting material and selective contact for high efficiency perovskite solar cells, Energy Environ. Sci. 9 (2016) 461–466.
[18] T.T. Duong, Q.D. Nguyen, S.K. Hong, D. Kim, T.H. Pham, S.G. Yoon, Enhanced photoelectrochemical activity of the TiO2/ITO nanocomposites grown onto single-walled carbon nanotubes at a low temperature by nanocluster deposition, Adv. Mater. 23 (46) (2011) 5557–5562.
[19] T.-V. Dang, S.V.N. Pammi, J. Choi, S.-G. Yoon, Utilization of AZO/Au/AZO multilayer electrodes instead of FTO for perovskite solar cells, Sol. Energy Mater. Sol. Cells 163 (2017) 58–65.
[20] W. Kwon, J.M. Kim, S.W. Rhee, Electrocatalytic carbonaceous materials for counter electrodes in dye-sensitized solar cells, J. Mater. Chem. 10 (2013) 3202–3215.
[21] P. Liu, Q. Sun, F. Zhu, K. Liu, K. Jiang, L. Liu, Q. Li, S. Fan, Measuring the work function of carbon nanotubes with thermionic method, Nano Lett. 8 (2008) 647–651.
[22] L. Kavan, N. Tétreault, T. Moehl, M. Grätzel, Electrochemical characterization of TiO2 blocking layers for dye-sensitized solar cells, J. Phys. Chem. C 118 (2014) 16408–16418.
[23] R.F. Michielli, P.J. Elving, Electrochemical reduction of benzophenone in aprotic medium. Effect of proton availability, J. Am. Chem. Soc. 90 (1968) 1989–1995.
[24] R.S. Nicholson, Theory and application of cyclic voltammetry for measurement of electrode reaction kinetics, Anal. Chem. 37 (1965) 1351–1355.
[25] L. Kavan, M. Grätzel, S.E. Gilbert, C. Klemenz, H.J. Scheel, Electrochemical and photoelectrochemical investigation of single-crystal anatase, J. Am. Chem. Soc. 118 (1996) 6716–6723.
[26] S. Lettieri, M. Pavone, A. Fioravanti, L.S. Amato, P. Maddalena, Charge carrier processes and optical properties in TiO_2 and TiO_2-based heterojunction photocatalysts: a review, Materials 14 (7) (2021) 1645.
[27] W. Chen, G.B. Huang, H. Song, J. Zhang, Efficient and stable charge transfer channels for photocatalytic water splitting activity of CdS without sacrificial agents, J. Mater. Chem. 8 (2020) 20963–20969.
[28] J. Li, X. Liu, J. Zhang, Smart assembly of sulfide heterojunction photocatalysts with well-defined interfaces for direct Z-scheme water splitting under visible light, ChemSusChem 13 (2020) 2996–3004.
[29] Y. Ma, H. Zhang, Y. Zhang, R. Hu, M. Jiang, R. Zhang, H. Lv, J. Tian, L. Chu, J. Zhang, Q. Xue, H.L. Yip, R. Xia, X. Li, W. Huang, Enhancing the performance of inverted perovskite solar cells via grain boundary passivation with carbon quantum dots, ACS Appl. Mater. Interfaces 11 (3) (2019) 3044–3052.
[30] A.K. Chandiran, A. Yella, M.T. Mayer, P. Gao, M.K. Nazeeruddin, M. Gratzel, Sub-nanometer conformal TiO_2 blocking layer for high efficiency solid-state perovskite absorber solar cells, Adv. Mater. 26 (2014) 4309.
[31] V.D. Dao, L. Larina, H.S. Choi, Minimizing energy losses in perovskite solar cells using plasma-treated transparent conducting layers, Thin Solid Films 593 (2015) 10–16.
[32] A. Dualeh, T. Moehl, N. Tétreault, J. Teuscher, P. Gao, M.K. Nazeeruddin, M. Gratzel, Impedance spectroscopic analysis of lead iodide perovskite-sensitized solid-state solar cells, ACS Nano 8 (2014) 362–373.